coatings

Communication

Microstructure Features and Mechanical Properties of Casted CoFeB Alloy Target

Ziyi Zhu [1,2], Jinjiang He [1,2,*], Yongjun Li [1,2], Junfeng Luo [1,2], Guojin Xu [1,2], Wenkui Yang [1,2], Dan Liu [1,2] and Jiali Gao [1,2]

[1] Grikin Advanced Materials Co., Ltd., Beijing Engineering Research Center of High Purity Metal Sputtering Targets, Beijing 102200, China; zhuzy@grikin.com (Z.Z.); lyj@grikin.com (Y.L.); ljf@grikin.com (J.L.); xgj@grikin.com (G.X.); ywk@grikin.com (W.Y.); liudan@grikin.com (D.L.); gaojiali@grikin.com (J.G.)
[2] National Engineering Research Center of Key Materials of Integrated Circuit, Beijing 100088, China
* Correspondence: hejinjiang@grikin.com

Abstract: CoFeB alloy, as a promising magneto-resistive material, has attracted extensive attention concerning the magnetic properties of its thin film in the field of magneto-resistive random memory (MRAM). Although there are many studies on the magnetic properties of CoFeB thin films, there is relatively little research on the microstructure and mechanical properties of casted CoFeB alloy. In this work, $Co_{20}Fe_{60}B_{20}$ (at%) alloy was fabricated through the vacuum induction melting method, and its microstructure features and mechanical performance were studied. Scanning electron microscopy (SEM), electron back scatter diffraction (EBSD), and transmission electron microscopy (TEM) were utilized to characterize the microstructure, which consists of the coarse, needle-like Fe_2B phase that crystallizes first, the primary lamellar binary eutectic structure (Fe_2B + bcc-Fe), and the ternary eutectic structure (Fe_3B + Fe_2B + bcc-Fe phase). It is found that Fe_3B precipitates on the Fe_2B with a core–shell structure. The orientation of bcc-Fe is randomly distributed, while there are two main kinds of textures in Fe_2B: {100} <001> and Gaussian texture {110} <001>. In terms of mechanical properties, $Co_{20}Fe_{60}B_{20}$ alloy's tensile strength is 140MPa, and the yield strength is 87MPa. Because the cracks are easy to generate and expand along the needle-shaped pre-crystallized Fe_2B, the plasticity of $Co_{20}Fe_{60}B_{20}$ alloy is very poor, only 1%.

Keywords: casted CoFeB alloy; magneto-resistive material; microstructure features; mechanical properties

Citation: Zhu, Z.; He, J.; Li, Y.; Luo, J.; Xu, G.; Yang, W.; Liu, D.; Gao, J. Microstructure Features and Mechanical Properties of Casted CoFeB Alloy Target. *Coatings* **2024**, *14*, 255. https://doi.org/10.3390/coatings14030255

Academic Editors: Francisco J. Flores-Ruiz and Saideep Muskeri

Received: 3 January 2024
Revised: 9 February 2024
Accepted: 13 February 2024
Published: 21 February 2024

1. Introduction

Nowadays, with the rise of big data-driven applications such as artificial intelligence (AI) and internet of things (IoT), the efficient transmission and processing of massive data have become a major challenge [1,2]. The growing demand for big-data storage and processing is limited by the von-Neumann architecture due to the memory bottleneck and power dissipation [3,4]. Taking advantage of nonvolatility, fast read/write speed, and low power, magnetic random access memory (MRAM) has become a promising candidate to overcome this limitation through processing-in-memory (PIM) architectures [5–9]. Based on the tunneling magneto-resistance effect (TMR) [10], two main generations of MRAM have been derived and commercially applied. The first generation is the magnetic field-driven MRAM, i.e., the magnetic field generated by the electric current drives the magnetic moment of the memory cell to perform the write operation, which is typically represented by the toggle-MRAM [11]. The second generation is the electric current-driven spin transfer torque MRAM (STT-MRAM), which means that the polarization electric current is used to perform the write operation on the memory cell. Due to the high density and fast write speed, the leading industries, such as Intel [12], Samsung [13], and GlobalFoundries [14], are releasing perpendicular STT-MRAM products as a cost-effective option for IoT, general-purpose microcontrollers, automotive, AI, and other low-power applications. However,

the basic storage unit of STT-MRAM is the magnetic tunnel junction (MTJ), which consists of a free layer, a tunnel gate, and a fixed layer [15]. CoFeB films exhibit excellent magnetic and electrical properties due to their amorphous structure and high spin polarization, and are widely used as free and pinned layers in STT-MRAM [16–20]. Currently, physical vapor deposition, especially magnetron sputtering, is commonly used to prepare MTJ thin film structures by setting a strong magnetic field on the backside of the CoFeB alloy target and increasing argon ionization to continuously bombard the target atoms to deposit thin films. The CoFeB alloy target mentioned in this work is the product obtained by welding CoFeB alloy with a copper or aluminum backing plate. The quality of target has a significant impact on the properties of the prepared films such as uniformity, thickness, etc. It can be seen that the CoFeB alloy target is the key raw material for the preparation of the MTJ free layer and pinned layer.

The studies [21–23] have performed a thermodynamic evaluation and calculated the liquid surface projection of the Co-Fe-B system, which was found to contain mainly the following phases: α-Fe, β-B, hcp-Co, (Fe,Co)B, $(Fe,Co)_2B$, and $(Fe,Co)_3B$. It has been reported that cobalt–boron alloy particles were found to be suitable for use as catalysts, magnetic materials, and coating materials with high corrosion resistance [24–26]. In addition, the cobalt–iron boron compounds formed by the addition of iron have a larger active surface area and better absorptive capacity, and have gained much attention in the field of catalysis [27]. Some CoFeB amorphous alloys are recommended for use in fine and tough magnetic coating materials [28]. However, as the key raw material for coating, the microstructure of CoFeB alloy, such as phase composition and distribution, extremely affects the sputtering coating effect, but the related literature published so far mainly focuses on the magnetic properties of CoFeB thin films [29–32], and the research results on the microstructure of raw casted CoFeB alloy are less published.

Therefore, in this paper, the microstructure of CoFeB alloy was studied in detail. The phase composition and the orientation relationship between phases and phases were analyzed by X-ray polycrystalline diffraction (XRD)/SEM/EBSD/TEM, and the mechanical properties of CoFeB alloy were investigated to provide a basis for the preparation and optimization of CoFeB alloy. Considering that $Co_{20}Fe_{60}B_{20}$ (at%) films are commonly used for the preparation of MTJ [33–36], this composition is adopted here.

2. Materials and Methods

$Co_{20}Fe_{60}B_{20}$ ingots with dimensions of 60 mm × 60 mm × 15 mm were prepared through vacuum induction melting (VIM). The crucible used was made of alumina with dimensions of φ 65 mm × 80 mm, and the mold used was copper with dimensions of 80 mm × 80 mm × 16 mm. High-purity argon gas of 0.06 atmospheres was passed during the melting process to prevent boron volatilization.

Samples of size 10 mm × 10 mm × 15 mm were cut and polished, then eroded with solution (hydrofluoric acid/nitric acid/sulfuric acid = 2:5:2) to prepare SEM/EBSD samples. TEM samples were prepared with a twin-jet polishing system (−20 °C, 5% perchloric acid methanol). The physical phase analysis was performed by XRD (Bruker D8, Cu target, Salbuluken, Germany), the morphology and composition analysis were performed by SEM (Zeiss ULTRA55, Jena, Germany), and the orientation relationship was analyzed by EBSD (Oxford C-NANO, Oxford, UK) and TEM (FEI Tecnai G20, Hillsboro, OR, USA). The tensile specimens (as shown in Figure 1) were polished with sandpaper from 60# to 600#, and the CMT4204 static hydraulic universal testing machine (Sansi Yongheng Technology, Ningbo, China) was used for tensile testing to determine the tensile strength, yield strength, and elongation to fracture. GB/T 228.1-2010 standard [37] was adopted and the displacement rate was 0.225 mm/min.

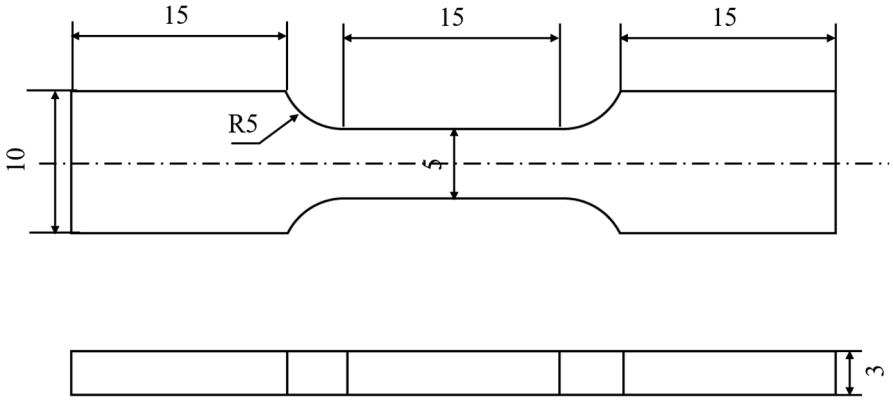

Figure 1. Diagram of tensile specimen.

3. Results and Discussions

3.1. Solidification Process Analysis

Figure 2a shows the Co-Fe-B ternary phase diagram, in which point A is the component point of $Co_{20}Fe_{60}B_{20}$, point B is the primary eutectic point, point C is the secondary eutectic point, and point D is the isotropic transition point of iron (912 °C, not identified in the figure). Figure 2b is a schematic diagram of the solidification process of $Co_{20}Fe_{60}B_{20}$ alloy in the equilibrium state. When cooling down from the liquid state, the following reactions will occur:

(1) A→B stage: When the melt cools, the component first passes through the Fe_2B solid-phase surface and crystallizes to form Fe_2B.

(2) B→C stage: When the melt continues to cool, it touches the intersection line of the Fe_2B and Fe (fcc, face-centered cubic). The first eutectic reaction L→Fe_2B + Fe(fcc) starts to occur. The phase composition is L, pre-crystalline Fe_2B, and primary eutectic organization (Fe_2B + Fe(fcc)) at this stage.

(3) C→D stage: When the melt continues to cool to the eutectic point C, the remaining liquid phase undergoes a secondary eutectic reaction: L→Fe_2B + Fe_3B + Fe(fcc). At this point, the liquid is consumed and completely transformed into a solid state, and the phase composition of the ingot is pre-crystalline Fe_2B, primary eutectic organization (Fe_2B + Fe(fcc)), and secondary eutectic organization (Fe_2B + Fe_3B + Fe(fcc). When the ingot temperature continues to decrease to the isotropic transition point D of Fe (913 °C), Fe(fcc) is converted to Fe (bcc, body-centered cubic).

3.2. Microstructure Features

Figure 3 shows the XRD pattern of the casted $Co_{20}Fe_{60}B_{20}$ alloy. The main phase composition includes Fe-bcc and Fe_2B (tetragonal, I-42m). The upper right corner in Figure 3 shows the crystal structure of Fe_2B in which the orange ball represents an iron atom and the black ball represents a boron atom. The peak of Fe_3B was not found in the XRD pattern, presumably due to the small amount of Fe_3B precipitation. The low Fe_3B content may be related to the use of copper mold cooling, which leads to the ingot being cooled too fast and thus solidifying in an unbalanced state. However, we discovered the presence of Fe_3B through the TEM method, which will be described subsequently.

Figure 4 shows the microstructure of the casted $Co_{20}Fe_{60}B_{20}$ alloy in SEM backscattering mode. The Fe_2B phase shows black contrast in the backscattering mode due to the higher percentage of B content than in the matrix. As shown in Figure 4, the microstructure of $Co_{20}Fe_{60}B_{20}$ alloy includes the pre-crystallized Fe_2B phase, the lamellar eutectic organization, and the point-like eutectic organization. The pre-crystallized Fe_2B phase is a coarse needle-like phase. This is due to the large temperature gradient caused by the excessive cooling speed of the copper mold casting, and then the pre-crystallized Fe_2B phase grows rapidly in the direction of the temperature gradient in a needle-like manner. In order to prove the accuracy of the analysis as above, we further performed the energy dispersive

spectrometer (EDS) analysis, as shown in Figure 5. It can be seen that the atom ratio of the needle phase is (Fe,Co)/B ≈ 2:1. It is worth mentioning that cobalt atoms displaced some of the iron atoms in the Fe_2B phase, causing lattice distortions but not changing the crystal structure of Fe_2B. Therefore, $(Fe,Co)_2B$ is abbreviated as Fe_2B in this work. Similarly, the (Fe,Co)B phase is abbreviated as FeB, and the $(Fe,Co)_3B$ phase is abbreviated as Fe_3B.

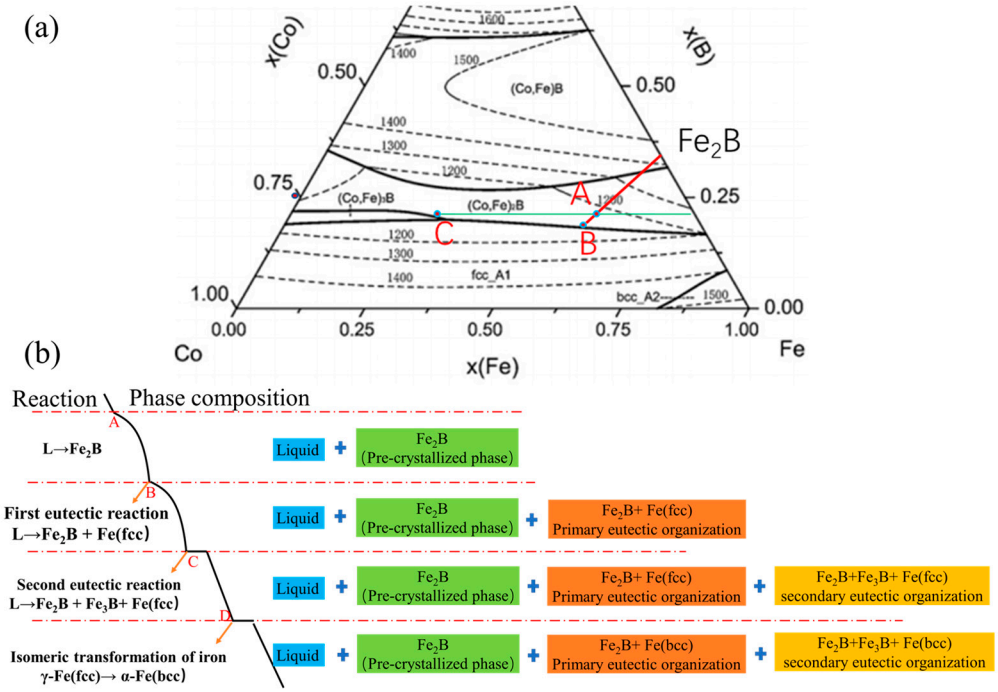

Figure 2. CoFeB alloy: (**a**) ternary phase diagram [21]; (**b**) equilibrium solidification process.

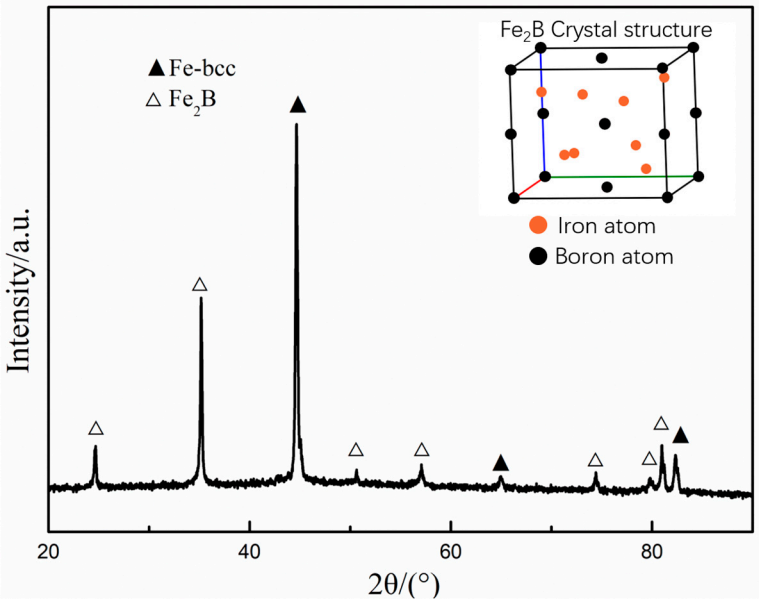

Figure 3. XRD pattern of casted $Co_{20}Fe_{60}B_{20}$ alloy.

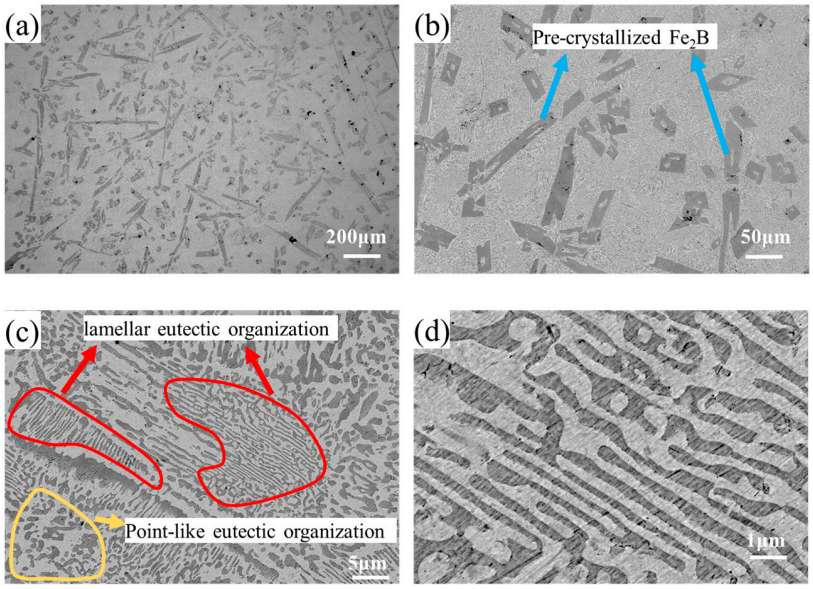

Figure 4. SEM backscattering mode analysis of casted CoFeB alloy: (**a**) 25×, (**b**) 100×, (**c**) 1000×, and (**d**) 5000×.

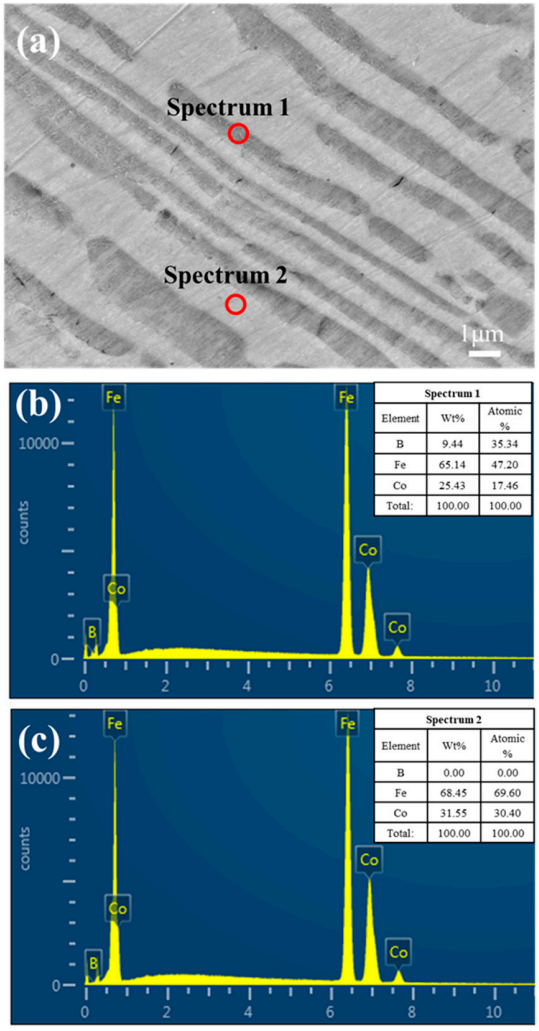

Figure 5. EDS analysis of the casted CoFeB alloy: (**a**) SEM map; (**b**) the EDS result of spectrum 1; (**c**) the EDS result of spectrum 2.

The lamellar eutectic organization was analyzed as a primary eutectic structure, as shown in Figure 4c,d, consisting of the black contrast Fe_2B phase and white contrast bcc-Fe phase. The first eutectic reaction (L→Fe_2B + Fe(fcc)) occurs when cooling from the liquid state to the eutectic composition point B, as shown in Figure 2b. Although both phases can be formed simultaneously, there is actually always one that is the leading crystalline phase. When the leading phase appears (assuming that the leading phase is the boron-rich Fe_2B phase), the liquid phase component on its side must be iron-rich, which induces the formation of the iron-rich bcc-Fe around Fe_2B phase. Similarly, the liquid phase around the iron-rich bcc-Fe phase must be rich in boron, which in turn prompts the boron-rich Fe_2B phase to form next to it, so that the two phases alternately promote each other, and finally form this lamellar eutectic organization. In addition, the point-like and lamellar organizations are considered to be the same kind. It is point-like due to the growth direction perpendicular to the observation surface. It can be seen that the micro-structure of $Co_{20}Fe_{60}B_{20}$ alloy mainly includes the pre-crystallized coarse needle-like Fe_2B phase and primary eutectic organization (Fe_2B + bcc-Fe), and no secondary eutectic organization is found, which is not easy to be detected by SEM. Boron-based coatings (e.g., FeB, Fe_2B, etc.) are commonly used in ferrous and non-ferrous metals and high-temperature alloys to improve the physicochemical properties of the material, especially in corrosive, thermal, and abrasive environments [38,39]. In the case of ferrous materials, boron particles diffuse on the surface of the material, filling the interstices of the substrate lattice and forming single-phase (FeB) or two-phase (FeB-Fe_2B) layers. The growth kinetics of the layers are temperature- and time-dependent, and layer thicknesses between 30 and 200 μm can be obtained [40]. However, in the casted CoFeB alloys, the Fe_2B phase is coarser, with a length of up to 400 μm, which is detrimental to the physical properties of the alloy.

Figure 6 shows the EBSD inverse pole figure (IPF) map and phase map of the casted CoFeB alloy. Based on the EBSD analysis, we further confirmed the phase compositions: bcc-Fe (blue) and Fe_2B (yellow). Fe_2B was distributed in long strips, with bcc-Fe distributed in between. The results show that the area proportion of Fe_2B is 29% and that of bcc-Fe is 71%.

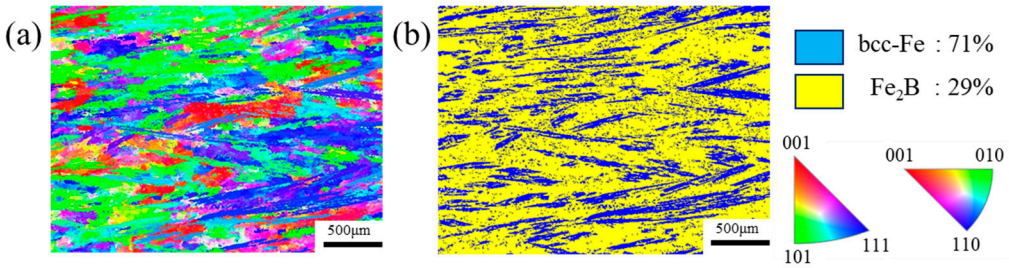

Figure 6. EBSD analysis of casted CoFeB alloy: (**a**) IPF map; (**b**) phase map.

Figure 7a shows the IPF diagram of bcc-Fe, while other phases are shown in white. Combined with the pole figures in Figure 7c, it can be seen that the grain orientation distribution of bcc-Fe is randomly distributed. Figure 7b is the IPF diagram of Fe_2B, while other phases are shown in white. Combined with the pole figure in Figure 7d, it can be seen that there are two main kinds of textures in Fe_2B: {100}<001> and Gaussian texture {110}<001>. The reasons for the formation of textures in Fe_2B are related to the rate of crystal growth during solidification, the action of heat flow, and differences in thermal conductivity in different crystallographic directions [41].

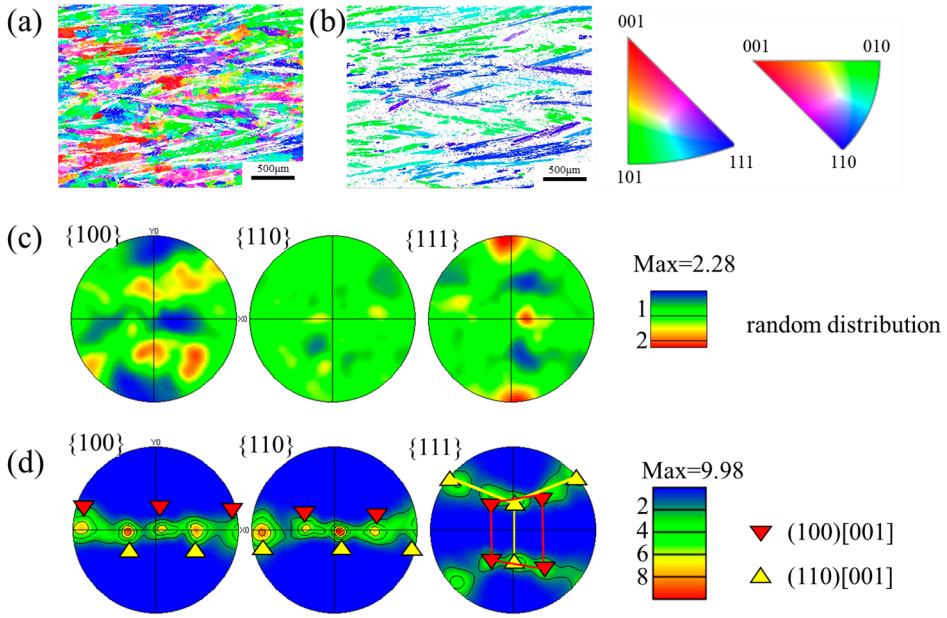

Figure 7. EBSD analysis of casted CoFeB alloy: (**a**) IPF map of bcc-Fe; (**b**) IPF map of Fe_2B; (**c**) pole figure of bcc-Fe; (**d**) pole figure of Fe_2B.

We further confirmed the existence of the Fe_3B through TEM analysis. From the selected diffraction of the area shown in the red circle of Figure 8a, it can be determined that Fe_3B (I-4 tetragonal) precipitates on the surface of Fe_2B in an encapsulated form and forms a core–shell structure, which can be treated as the secondary eutectic organization shown in Figure 2b. It is worth mentioning that the thin layer structure of Fe_3B is only 30–50 nm thick, which is not easily detected in SEM. Fe_2B and Fe_3B are both hard and brittle phases, and this encapsulated structure will further reduce the plasticity of the alloy. In addition, the following orientation relationship exists: (21-1) Fe_3B//(-200) bcc-Fe, as shown in Figure 8d. Core–shell structures are a class of particles consisting of two or more distinct layers of material. One of them forms the inner core and the others form the outer layer or shell [42,43]. This type of design provides the opportunity to tune composites to have properties and performance that cannot be achieved with the individual materials of the core and shell. Some researchers have implemented different solidification conditions to prevent coarsening by using intrinsic heat treatment (IHT) to form a zirconium-rich shell around AlSc precipitates. This approach is applicable to a wide range of precipitation-hardened alloys to trigger in situ precipitation [44,45]. In this casted CoFeB alloy, the Fe_3B phase precipitates in a core–shell over the Fe_2B phase, which prevents the Fe_2B phase from growing too large. In any case, under the present experimental conditions, there is less of this core–shell structure, so the Fe_2B phase essentially precipitates as a coarse needle-like phase.

Figure 9a shows the TEM bright-field image of the casted $Co_{20}Fe_{60}B_{20}$ alloy. A large number of stacking faults are observed in bcc-Fe, which may be a result of the fast-cooling rate leading to the initiation of incomplete dislocations in bcc-Fe to coordinate the stress. From the diffraction spot calibration results of Figure 9b, it can be seen that the long strip of the second phase is Fe_2B, which will significantly reduce the mechanical properties of the alloy since Fe_2B is a hard and brittle phase. As shown in Figure 10, there are substructures inside the Fe_2B, and there is a 3° orientation angle between the substructures.

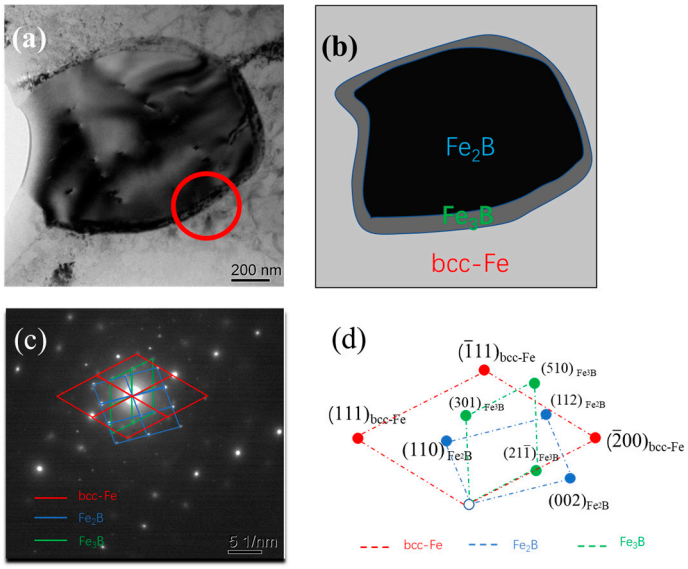

Figure 8. TEM analysis: (**a**) bright-field image; (**b**) phase distribution schematic; (**c**) diffraction spot; (**d**) diffraction spot calibration.

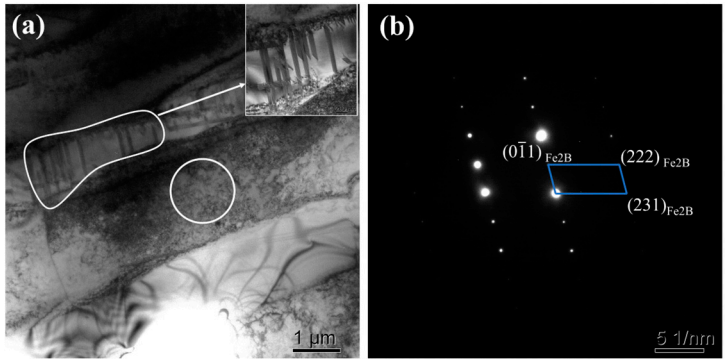

Figure 9. TEM analysis: (**a**) bright-field image; (**b**) diffraction spot in the area shown by circles in (**a**).

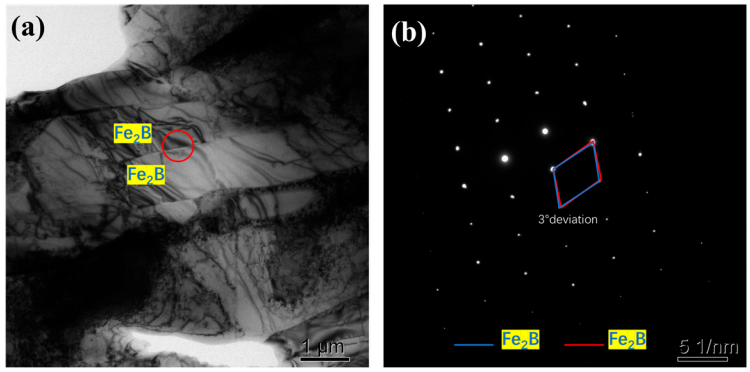

Figure 10. TEM analysis: (**a**) bright-field image; (**b**) diffraction spot calibration.

3.3. Mechanical Properties

Figure 11 shows the tensile test results of $Co_{20}Fe_{60}B_{20}$ alloy. It can be seen that it has poor room-temperature tensile properties, with a tensile strength of 140 MPa, yield strength of 87 MPa, and elongation of only 1%. The hard and brittle Fe_2B phase is interspersed in the bcc-Fe matrix, causing the alloy to crack easily along the hard and brittle second phase during plastic deformation. Figure 12 shows the fracture morphology of the tensile specimens, which shows that the samples undergo brittle cleavage fracture at the location

of the Fe_2B phase. It is widely recognized that the deconvoluted fracture of steel is related to the carbide precipitates. For example, brittle second-phase particles such as carbides in ferritic/martensitic steels are potential nucleation sources for deconvoluted fracture [46]. During the loading process, brittle particles in the high-stress region may fracture and form microcracks. These microcracks can even extend to neighboring grains, although the crack extension can be prevented by grain boundaries. With further development of the extension process, unstable deconvoluted fracture occurs, leading to catastrophic structural damage. Based on the above microstructure analysis, we suggest that the main reasons for such poor physical properties are as follows: (1) the coarse hard and brittle phase Fe_2B precipitates in the form of needles; (2) the Fe_3B phase wraps around the Fe_2B surface, and the junction of the two phases is more likely to produce cracks.

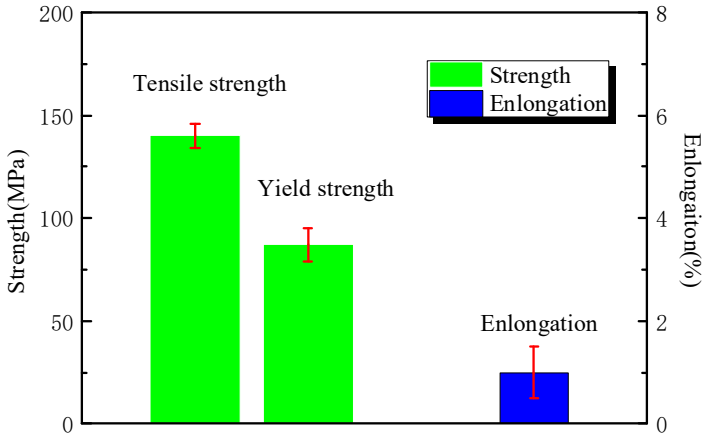

Figure 11. Tensile test results of $Co_{20}Fe_{60}B_{20}$ alloy.

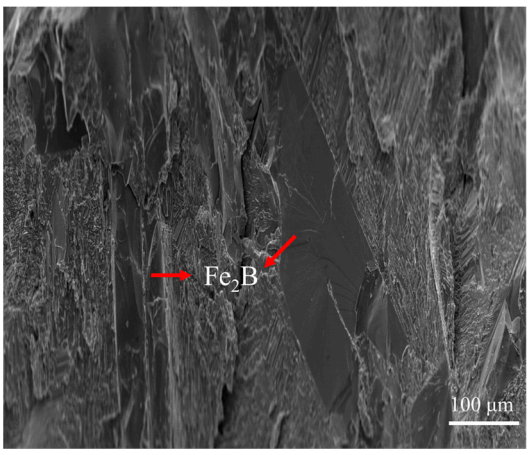

Figure 12. SEM image of tensile fracture morphology.

In summary, $Co_{20}Fe_{60}B_{20}$ alloy has very poor mechanical properties at room temperature. The next focus will be to study the effect of cooling rate and the direction of the temperature gradient on the orientation of the first precipitated phase and the elimination of the core–shell structure to improve the mechanical properties of the CoFeB alloy target.

4. Conclusions

In this study, the microstructure and mechanical properties of casted $Co_{20}Fe_{60}B_{20}$ alloy prepared through vacuum induction melting were investigated, and this can provide guidance for the preparation of CoFeB alloy targets. The conclusions obtained were as follows:

(1) The microstructure of $Co_{20}Fe_{60}B_{20}$ alloy consists of a coarse, needle-like Fe_2B phase that crystallizes first, a primary lamellar eutectic organization (Fe_2B + bcc-Fe), and a secondary eutectic organization (Fe_3B + Fe_2B + bcc-Fe phase, in which Fe_3B precipitates on the surface of the Fe_2B in a core–shell form).
(2) The orientation of bcc-Fe is randomly distributed, while there are two main kinds of textures in Fe_2B: {100} <001> and Gaussian texture {110} <001>.
(3) The $Co_{20}Fe_{60}B_{20}$ alloy has poor mechanical properties at room temperature, with a tensile strength of 140 MPa, yield strength of 87 MPa, and elongation of 1% only. The reasons for the poor plasticity of the $Co_{20}Fe_{60}B_{20}$ alloy are as follows: (1) the hard and brittle Fe_2B precipitates in the form of needles; (2) Fe_3B precipitates on the surface of Fe_2B in a core–shell form, and cracks tend to form at the phase interface.

Author Contributions: Writing—original draft, Z.Z.; conceptualization, J.H.; methodology Y.L.; investigation, J.L.; validation G.X.; writing—review and editing, W.Y.; visualization, J.G.; resources, D.L. All authors have read and agreed to the published version of the manuscript.

Funding: This work was funded by the National Key R&D Program of China (No. 2022 YFB3504403).

Institutional Review Board Statement: Not applicable.

Informed Consent Statement: Not applicable.

Data Availability Statement: The data that support the findings of this study are available on request from the corresponding author.

Conflicts of Interest: Authors Ziyi Zhu, Jinjiang He, Yongjun Li, Junfeng Luo, Guojin Xu, Wenkui Yang, Dan Liu and Jiali Gao were employed by the company Grikin Advanced Materials Co., Ltd. And authors declare that the research was conducted in the absence of any commercial or financial relationships that could be construed as a potential conflict of interest.

References

1. Khoram, S.; Zha, Y.; Zhang, J.; Li, J. Challenges and opportunities: From near-memory computing to in-memory computing. In Proceedings of the 2017 ACM on International Symposium on Physical Design, Portland, OR, USA, 19–22 March 2017; pp. 43–46. [CrossRef]
2. Dieny, B.; Prejbeanu, I.L.; Garello, K.; Gambardella, P.; Freitas, P.; Lehndorff, R.; Raberg, W.; Ebels, U.; Demokritov, S.O.; Akerman, J.; et al. Opportunities and challenges for spintronics in the microelectronics industry. *Nat. Electron.* **2020**, *3*, 446–459. [CrossRef]
3. Kim, N.S.; Austin, T.; Baauw, D.; Mudge, T.; Flautner, K.; Hu, J.S.; Irwin, M.; Kandemir, M.; Narayanan, V. Leakage current: Moore's law meets static power. *Computer* **2003**, *36*, 68–75. [CrossRef]
4. Kuroda, T. Low-power, high-speed CMOS VLSI design. In Proceedings of the IEEE International Conference on Computer Design: VLSI in Computers and Processors, Freiburg, Germany, 18 September 2002; IEEE: Piscataway, NJ, USA, 2002; pp. 310–315. [CrossRef]
5. Khvalkovskiy, A.V.; Apalkov, D.; Watts, S.; Chepulskii, R.; Beach, R.S.; Ong, A.; Tang, X.; Driskill-Smith, A.; Butler, W.H.; Visscher, P.B. Erratum: Basic principles of STT-MARM cell operation in memory arrays. *J. Phys. D Appl. Phys.* **2013**, *46*, 074001. [CrossRef]
6. Tsuchida, K.; Inaba, T.; Fujita, K.; Ueda, Y.; Shimizu, T.; Asao, Y.; Kajiyama, T.; Iwayama, M.; Sugiura, K.; Ikegawa, S.; et al. A 64Mb MRAM with clamped-reference and adequate-reference schemes. In Proceedings of the 2010 IEEE International Solid-State Circuits Conference—(ISSCC), San Francisco, CA, USA, 7–11 February 2010; pp. 258–259. [CrossRef]
7. Hirohata, A. MRAM makes its mark. *Nat. Electron.* **2022**, *5*, 832–833. [CrossRef]
8. Guo, Z.X.; Yin, J.L.; Bai, Y.; Zhu, D.Q.; Shi, K.; Wang, G.; Cao, K.; Zhao, W.S. Spintronics for Energy-Efficient Computing: An Overview and Outlook. *Proc. IEEE* **2021**, *109*, 1398–1417. [CrossRef]
9. Shao, Q.M.; Li, P.; Liu, P.; Yang, H.; Fukami, S.; Razavi, A.; Wu, H.; Wang, K.; Freimuth, F.; Mokrousov, Y.; et al. Roadmap of Spin–Orbit Torques. *IEEE Trans. Magn.* **2021**, *57*, 800439. [CrossRef]
10. Zhang, Y.; Wang, Y.Z.; Han, X.F.; Deng, H.; Huang, H.; Guo, J.; Liang, Y.; Si, W.; Jiang, A.; Liu, H.; et al. Electron irradiation total ionizing dose (TID) effect of tunneling magnetoresistance sensors. *J. Magn. Magn. Mater.* **2022**, *563*, 169954. [CrossRef]
11. Wang, J.; Lian, C.; Bai, Y.; Wang, G.; Zhang, Z.; Zheng, Z.; Chen, L.; Lin, K.; Zhang, K.; Zhang, Y.; et al. A self-matching complementary-reference sensing scheme for high-speed and reliable toggle spin torque MRAM. *IEEE Trans. Circuits Syst. I* **2020**, *67*, 4247–4258. [CrossRef]
12. Alzate, J.G.; Arslan, U.; Bai, P.; Brockman, J.; Chen, Y.J.; Das, N.; Fischer, K.; Ghani, T.; Heil, P.; Hentges, P.; et al. 2 MB array-level demonstration of STT-MRAM process and performance towards L4 cache applications. In Proceedings of the 2019 IEEE International Electron Devices Meeting (IEDM), San Francisco, CA, USA, 7–11 December 2019; pp. 2.4.1–2.4.4. [CrossRef]

13. Park, J.H.; Lee, J.; Jeong, J.; Pi, U.; Kim, W.; Lee, S.; Noh, E.; Kim, K.; Lim, W.C.; Kwon, S.; et al. A novel integration of STT-MRAM for on-chip hybrid memory by utilizing non-volatility modulation. In Proceedings of the 2019 IEEE International Electron Devices Meeting (IEDM), San Francisco, CA, USA, 7–11 December 2019; pp. 2.5.1–2.5.4. [CrossRef]
14. Lee, K.; Chao, R.; Yamane, K.; Naik, V.B.; Yang, H.; Kwon, J.; Chung, N.L.; Jang, S.H.; Behin-Aein, B.; Lim, J.; et al. 22-nm FD-SOI embedded MRAM technology for low-power automotive-grade-l MCU applications. In Proceedings of the 2018 IEEE International Electron Devices Meeting (IEDM), San Francisco, CA, USA, 1–5 December 2018; pp. 27.1.1–27.1.4. [CrossRef]
15. Ferdaus, F.; Bahar Talukder, B.M.S.; Sadi, M.; Rahman, M.T. True Random Number Generation using Latency Variations of Commercial MRAM Chips. In Proceedings of the 22nd International Symposium on Quality Electronic Design (ISQED), Santa Clara, CA, USA, 7–9 April 2021; pp. 510–515. [CrossRef]
16. Na, T.; Kang, S.H.; Jung, S.O. STT-MRAM sensing: A review. *IEEE Trans. Circuits Syst. II Express Briefs* **2020**, *68*, 12–18. [CrossRef]
17. Ikeda, S.; Miura, K.; Yamamoto, H.; Mizunuma, K.; Gan, H.; Endo, M.; Kanai, S.; Hayakawa, J.; Matsukura, F.; Ohno, H. A perpendicular-anisotropy CoFeB–MgO magnetic tunnel junction. *Nat. Mater.* **2010**, *9*, 721–724. [CrossRef] [PubMed]
18. Sato, H.; Yamanouchi, M.; Ikeda, S.; Fukami, S.; Matsukura, F.; Ohno, H. Perpendicular-anisotropy CoFeB-MgO magnetic tunnel junctions with a MgO/CoFeB/Ta/CoFeB/MgO recording structure. *Appl. Phys. Lett.* **2012**, *101*, 022414. [CrossRef]
19. Li, H.; Xie, Y.; Yang, H.; Hu, H.; Li, M.; Li, R.-W. The Effect of Size and Strain on Micro Stripe Magnetic Domain Structure of CoFeB Thin Films. *Metals* **2023**, *13*, 678. [CrossRef]
20. Son, H.; Park, J.; Lee, H.; Choi-Yim, H. Annealing Effect in Amorphous Fe-Co-B-Si-Nb According to Fe/Co Ratio. *Metals* **2023**, *13*, 715. [CrossRef]
21. Liu, Y.Q.; Zhao, X.S.; Yang, J.; Shen, J.Y. Thermodynamic optimization of the boron–cobalt–iron system. *J. Alloys Compd.* **2011**, *509*, 4805–4810. [CrossRef]
22. Raghavan, V. B-Co-Fe (boron-cobalt-iron). *J. Phase Equilibria Diffus.* **2012**, *33*, 392–394. [CrossRef]
23. Wallisch, W.; Fidler, J.; Toson, P.; Sassik, H.; Svagera, R.; Bernardi, J. Synthesis and characterization of (Fe, Co) 2–3B microcrystalline alloys. *J. Alloys Compd.* **2015**, *644*, 199–204. [CrossRef]
24. Rinaldi, A.; Correa-Duarte, M.A.; Salgueirino-Maceira, V.; Licoccia, S.; Traversa, E.; Dávila-Ibáñez, A.; Peralta, P.; Sieradzki, K. Elastic properties of hard cobalt boride composite nanoparticles. *Acta Mater.* **2010**, *58*, 6474–6486. [CrossRef]
25. Li, X.; Wang, C.; Han, X.; Wu, Y. Surfactant-free synthesis and electromagnetic properties of Co–Ni–B composite particles. *Mater. Sci. Eng. B* **2013**, *178*, 211–217. [CrossRef]
26. Euchner, H.; Mayrhofer, P.H. Designing thin film materials—Ternary borides from first principles. *Thin Solid Films* **2015**, *583*, 46–49. [CrossRef] [PubMed]
27. Klemenz, S.; Schuch, J.; Hawel, S.; Zieschang, A.; Kaiser, B.; Jaegermann, W.; Albert, B. Synthesis of a Highly Efficient Oxygen-Evolution Electrocatalyst by Incorporation of Iron into Nanoscale Cobalt Borides. *ChemSusChem* **2018**, *11*, 3150–3156. [CrossRef] [PubMed]
28. Wells, J.; Lee, J.H.; Mansell, R.; Cowburn, R.; Kazakova, O. Controlled manipulation of domain walls in ultra-thin CoFeB nanodevices. *J. Magn. Magn. Mater.* **2016**, *400*, 219–224. [CrossRef]
29. Kim, J.S.; Kim, G.; Jung, J.; Jung, K.; Cho, J.; Kim, W.-Y.; You, C.-Y. Control of crystallization and magnetic properties of CoFeB by boron concentration. *Sci. Rep.* **2022**, *12*, 4549. [CrossRef]
30. Li, Z.P.; Li, S.; Zheng, Y.; Fang, J.; Chen, L.; Liang, H.; Wang, H. The study of origin of interfacial perpendicular magnetic anisotropy in ultra-thin CoFeB layer on the top of MgO based magnetic tunnel junction. *Appl. Phys. Lett.* **2016**, *109*, 182403. [CrossRef]
31. Cho, J.H.; Jung, J.Y.; Cho, S.Y.; You, C.Y. Effect of annealing temperature on exchange stiffness of CoFeB thin films. *J. Magn. Magn. Mater.* **2015**, *395*, 18–22. [CrossRef]
32. Bilzer, C.; Devolder, T.; Kim, J.V.; Counil, G.; Chappert, C.; Cardoso, S.; Freitas, P.P. Study of the dynamic magnetic properties of soft CoFeB films. *J. Appl. Phys.* **2006**, *100*, 053903. [CrossRef]
33. Lkeda, S.; Hayakawa, J.; Ashizawa, Y.; Lee, Y.M.; Miura, K.; Hasegawa, H.; Tsunoda, M.; Matsukura, F.; Ohno, H. Tunnel magnetoresistance of 604% at 300K by suppression of Ta diffusion in CoFeB/MgO/CoFeB pseudo-spin-valves annealed at high temperature. *Appl. Phys. Lett.* **2008**, *93*, 082508. [CrossRef]
34. Harres, A.; Mallmann, T.A.; Gamino, M.; Correa, M.A.; Viegas, A.D.C.; da Silva, R.B. Magnetization reversal processes in amorphous CoFeB thin films. *J. Magn. Magn. Mater.* **2022**, *552*, 169135. [CrossRef]
35. Xu, Z.; Qin, L. Effects of sputtering parameters and annealing temperatures on magnetic properties of CoFeB films. *J. Magn. Magn. Mater.* **2021**, *538*, 168302. [CrossRef]
36. Liu, B.H.; Taiebeh, T.; Kenny, O.; Hanwei, T.; Mo, Z.Q.; Jeffrey, L.; Pik, K.T.; Zhao, Y.Z.; Dong, Z.L.; Dimitri, H.; et al. Electron radiation-induced material diffusion and nanocrystallization in nanostructured amorphous CoFeB thin film. *Acta Mater.* **2018**, *161*, 221–236. [CrossRef]
37. *GB/T 228.1-2010*; Metallic Materials—Tensile Testing—Part 1: Method of Test at Room Temperature. Ministry of Communi-cations of the PRC: Beijing, China, 2010.
38. García-Léon, R.A.; Martínez-Trinidad, J.; Campos-Silva, I.; Wong-Angel, W. Mechanical characterization of the AISI 316L alloy exposed to boriding process. *DYNA* **2020**, *87*, 34–41. [CrossRef]
39. Özbek, I.; Konduk, B.; Bindal, C.; Ucisik, A. Characterization of borided AISI 316L stainless steel implant. *Vacuum* **2022**, *65*, 521–525. [CrossRef]

40. Martini, C.; Palombarini, G.; Carbucicchio, M. Mechanism of thermochemical growth of iron borides on iron. *J. Mater. Sci.* **2024**, *39*, 933–937. [CrossRef]
41. Ahmed, T.; David, W.G.; Suraj, M.V.; Ohodnicki, P.R. Electromagnetic assisted thermal processing of amorphous and nanocrystalline soft magnetic alloys: Fundamentals and advances. *J. Alloys Compd.* **2021**, *854*, 156480. [CrossRef]
42. Hayes, R.; Ahmed, A.; Edge, T.; Zhang, H. Core-shell particles: Preparation, fundamentals and applications in high performance liquid chromatography. *J. Chromatogr. A* **2014**, *1357*, 36–52. [CrossRef]
43. Ramli, R.A.; Laftah, W.A.; Hashim, S. Core-shell polymers: A review. *RSC Adv.* **2013**, *3*, 15543–15565. [CrossRef]
44. Sun, N.; Xiao, Z. Synthesis and performances of phase change materials microcapsules with a polymer/BN/TiO_2 hybrid shell for thermal energy storage. *Energy Fuels* **2017**, *31*, 10186–10195. [CrossRef]
45. Akamatsu, K.; Yamaguchi, T. Novel preparation method for obtaining pH-responsive Core-shell microcapsule reactors. *Ind. Eng. Chem. Res.* **2007**, *46*, 124–130. [CrossRef]
46. Chen, L.; Liu, W.; Yu, L.; Cheng, Y.; Ren, K.; Sui, H.; Yi, X.; Duan, H. Probabilistic and constitutive models for ductile-to-brittle transition in steels: A competition between cleavage and ductile fracture. *J. Mech. Phys. Solids* **2020**, *135*, 103809. [CrossRef]